ADVANCED FUNCTIONAL MATERIALS
www.afm-journal.de

Tuning Spin-Orbit Torques Across the Phase Transition in VO_2/NiFe Heterostructure

*Jun-young Kim, Joel Cramer, Kyujoon Lee, Dong-Soo Han, Dongwook Go, Pavel Salev, Pavel N. Lapa, Nicolas M. Vargas, Ivan K. Schuller, Yuriy Mokrousov, Gerhard Jakob, and Mathias Kläui**

The emergence of spin-orbit torques as a promising approach to energy-efficient magnetic switching has generated large interest in material systems with easily and fully tunable spin-orbit torques. Here, current-induced spin-orbit torques in VO_2/NiFe heterostructures are investigated using spin-torque ferromagnetic resonance, where the VO_2 layer undergoes a prominent insulator-metal transition. A roughly twofold increase in the Gilbert damping parameter, α, with temperature is attributed to the change in the VO_2/NiFe interface spin absorption across the VO_2 phase transition. More remarkably, a large modulation (±100%) and a sign change of the current-induced spin-orbit torque across the VO_2 phase transition suggest two competing spin-orbit torque generating mechanisms. The bulk spin Hall effect in metallic VO_2, corroborated by the first-principles calculation of the spin Hall conductivity $\sigma_{SH} \approx -10^4 \left(\frac{\hbar}{e}\right) \Omega^{-1}\,m^{-1}$, is verified as the main source of the spin-orbit torque in the metallic phase. The self-induced/anomalous torque in NiFe, with opposite sign and a similar magnitude to the bulk spin Hall effect in metallic VO_2, can be the other competing mechanism that dominates as temperature decreases. For applications, the strong tunability of the torque strength and direction opens a new route to tailor spin-orbit torques of materials that undergo phase transitions for new device functionalities.

1. Introduction

Long-term goals of spintronics are the generation and the utilization of spin currents for information processing and storage.[1,2] Compared to optical and electrical spin injection schemes,[3,4] the spin current generation via spin-orbit interaction has demonstrated efficient charge-to-spin conversion[5,6] and has received much interest not only in the fundamental understanding but also in particular for technological applications. Notably, magnetization switching via spin-orbit torques[7,8] offers a number of advantages over conventional spin-transfer torque switching and is actively being developed into new generation spintronics devices such as spin-orbit torque magnetoresistance random access memory.[9]

The main mechanisms behind these recent advances are the current-induced spin-orbit torques.[10,11] The torques can be realized in a number of different ferromagnet–nonmagnet systems, and efficient charge-to-spin conversion was observed not only in conventional metallic heterostructures but also in nonmagnetic metal bilayers,[12] semiconductor quantum wells,[13–15] and topological insulators.[16–18] So far various mechanisms for the observed spin-orbit torques have been identified; however, very often it has been challenging to identify the origin of the spin-orbit torques because different mechanisms contribute at the same time and compete with each other. Furthermore, varying layer thicknesses in order to disentangle bulk and interface effects poses difficulties as the growth

J.-y. Kim, J. Cramer, K. Lee, D.-S. Han, D. Go, Y. Mokrousov, G. Jakob, M. Kläui
Institute of Physics
Johannes Gutenberg University
Mainz 55128, Germany
E-mail: mathias.klaeui@magnetism.ch

J.-y. Kim
Max Planck Institute for Intelligent Systems
Stuttgart 70569, Germany

The ORCID identification number(s) for the author(s) of this article can be found under https://doi.org/10.1002/adfm.202111555.

DOI: 10.1002/adfm.202111555

K. Lee
Department of Semiconductor Physics
Korea University
Sejong 30019, Republic of Korea

D.-S. Han
Korea Institute of Science and Technology
Seoul 02792, Republic of Korea

D. Go, Y. Mokrousov
Peter Grünberg Institut and Institute for Advanced Simulation
Forschungszentrum Jülich and JARA
Jülich 52425, Germany

P. Salev, P. N. Lapa, N. M. Vargas, I. K. Schuller
Department of Physics and Center for Advanced Nanoscience
University of California San Diego
La Jolla, CA 92093, USA

and interface properties change with varying thicknesses. For the bulk effects, the spin Hall effect of the nonmagnet has been regarded as one of the main contributions and the values can now also be calculated theoretically.[6,8] Meanwhile, although the effect of spin-orbit coupling in the ferromagnet has been regarded as negligible so far, a recent experiment[19] revealed that even a single ferromagnet can generate substantial self-induced torque with a defined sign. Moreover, it was shown that orbital Hall currents generated from the nonmagnetic layer can also contribute strongly to the torque.[20]

The spin-orbit torque efficiency is a parameter that is usually set for a specific material and interface, and it cannot be modulated easily. While it has been recently shown that strain can be used to control the spin-orbit torque to some extent,[21] a piezoelectric substrate is often required that complicates growth and optimization of thin films. In this respect, an interesting material is vanadium dioxide (VO_2), a transition metal oxide that undergoes a prominent insulator–metal transition with temperature. The hysteretic phase transition allows to deliberately switch between insulating and metallic states, which can then influence the current flow and thus spin-orbit effects. The change in the VO_2 orbital occupation[22] across the structural phase transition leads to the large changes in electrical resistivity[23] as well as optical,[24] structural,[25] and magnetic properties[26–28] and is expected to affect the spin-orbit coupling directly.[29] However, the effect of the VO_2 phase transition on current-induced spin-orbit torques in a VO_2/ferromagnet heterostructure, which is of key importance for the future functionalization, has not been investigated and therefore is the main focus of this study.

In this work, we investigate current-induced spin-orbit torques in a VO_2/NiFe heterostructure across the VO_2 insulator–metal phase transition with the emphasis on the functionalization. The sign and the magnitude of the generated spin-orbit torques are probed using the spin-torque ferromagnetic resonance (ST-FMR) technique, where we inspect resonance linewidths of the bilayer strips with an additional DC current through the strip. Due to the several orders of magnitude changes in the electrical resistivity of the VO_2 layer across the phase transition, the ratio of the applied charge currents in the VO_2 and the NiFe layers is thus controlled by changing temperature. In particular, we quantify the large variation including a sign change of spin-orbit torque in different VO_2 phases. The observed hysteretic, phase-dependent spin-orbit torques could be utilized for future device concepts.

2. ST-FMR Measurements Across Insulator–Metal Transition

First, several structural characterizations were performed to inspect the quality of the VO_2 films. **Figure 1**a shows an out-of-plane x-ray diffraction plot of the 70 nm thick VO_2 film deposited by reactive sputtering on Al_2O_3(1-102). The (110), (200), and (111) VO_2 peaks are visible, indicating the polycrystalline growth of the VO_2 film. In Figure 1b, a 1 µm × 1 µm atomic force microscopic image of the same film shows large structural domains of a few hundred nanometer sizes with a root-mean-square roughness of 6.3 nm. Figure 1c displays the temperature

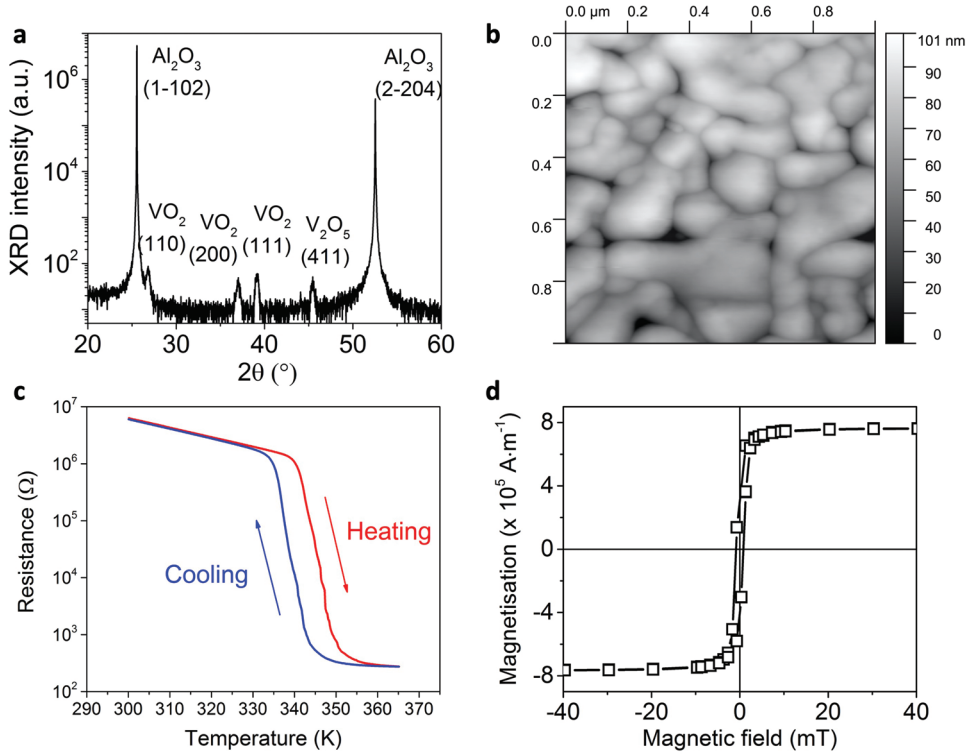

Figure 1. Structural properties and insulator-metal transition of VO_2. a) Out-of-plane XRD scan of the 70 nm VO_2 film on the Al_2O_3(1-102) substrate. b) 1 µm × 1 µm atomic force micrograph and c) temperature dependence of four-probe van der Pauw resistance of the VO_2 film. d) SQUID *M-H* loops of the VO_2 (70 nm)/NiFe (5 nm) bilayer measured at 300 K.

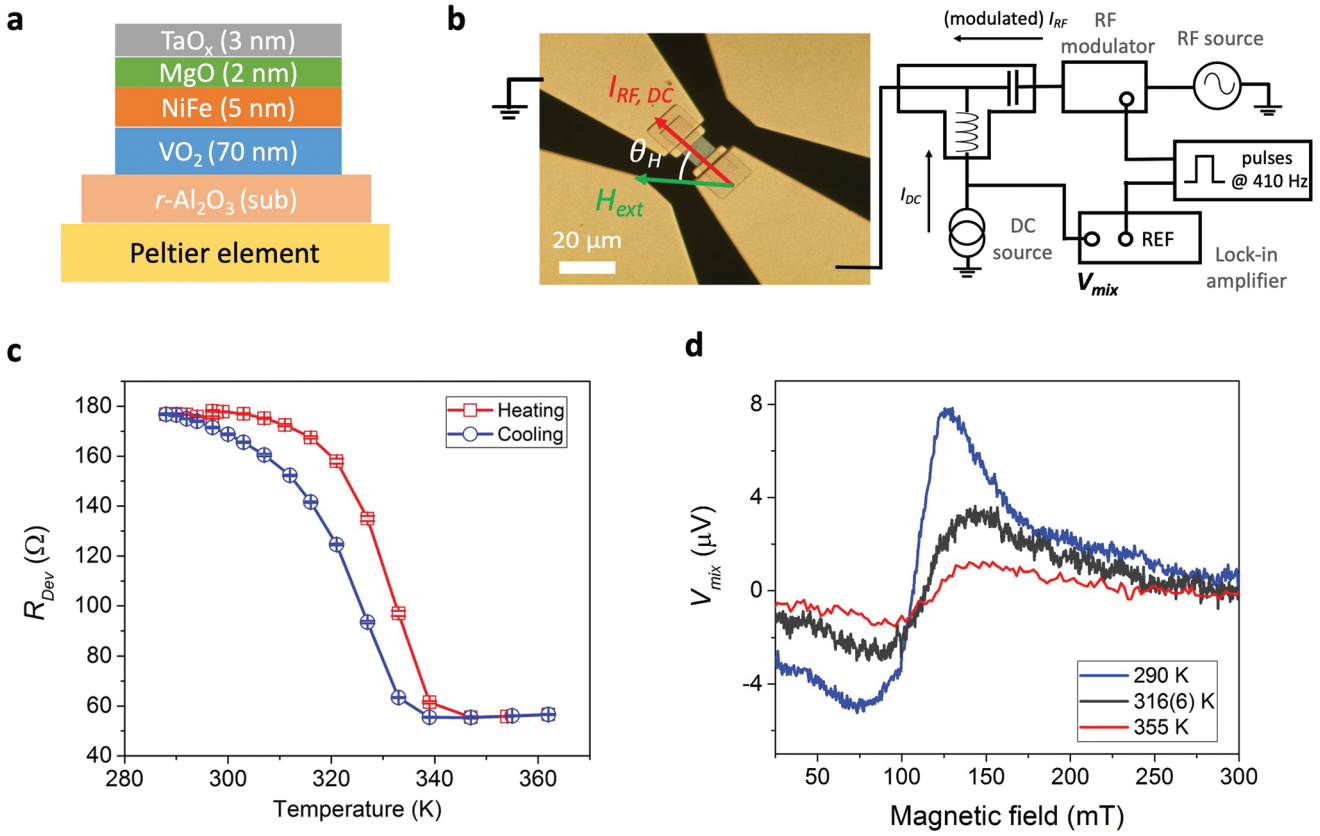

Figure 2. VO_2/NiFe bilayer sample and ST-FMR measurements. a) Cross section of the studied heterostructure and microscope image of the 10 µm-wide device embedded into the CPW circuit. b) The experimental setup used for ST-FMR measurements. θ_H defines the angle between the external magnetic field, H_{ext}, and the direction of an electric current, I_{RF} and I_{DC}. c) Temperature dependence of the device resistance. In order to distinguish the hysteretic effects, the resistances measured during heating (red) and cooling (blue) are indicated. d) ST-FMR field sweep spectra with 8 GHz, 3 dBm RF excitation at the sample temperatures of 290 K (blue), (316 ± 6) K (dark grey) and 355 K (red).

dependence of van der Pauw resistance of the as-deposited VO_2 film, where an insulator–metal transition with temperature results in a resistance change of four orders of magnitude, as observed previously.[23] In order to characterize the current-induced spin-orbit torques of the VO_2 layers, a $Ni_{81}Fe_{19}$ (5 nm)/MgO (2 nm)/Ta (3 nm) multilayer stack is sputter-deposited on top of the VO_2 (70 nm) film. *M-H* hysteresis loops of the resulting multilayer stack measured at 300 K are shown in Figure 1d. The magnetically soft NiFe layer is fully saturated by a 10 mT magnetic field to within 10% of the expected bulk saturation value of ≈ 8.8 × 10^5 A m^{-1}, with a coercivity less than 1 mT.

The VO_2/NiFe/MgO/Ta structure (**Figure 2**a) is patterned into a 10 µm wide strip and embedded into a coplanar-waveguide circuit, as seen in the measurement schematic in Figure 2b. Details of the patterning process can be found in the Supporting Information Section II. The temperature-dependent resistance of the patterned device stack is shown in Figure 2c. In the patterned strip, the insulator–metal transition becomes broader in temperature than in the unpatterned film (Figure 1c), which we account to edge defects created during the patterning process. ST-FMR field sweeps of the sample measured at different sample temperatures between 290 and 355 K are shown in Figure 2d. The sample temperatures were controlled using a Peltier element directly under the sample. The ST-FMR signal, V_{mix}, which effectively measures the RF-current-rectified anisotropic magnetoresistance of the strip, is enhanced when the applied magnetic field and the RF current frequency matches the resonance condition for the NiFe moment precession. The obtained ST-FMR line shape can be represented as a superposition of symmetric and antisymmetric Lorentzian components using the equation[30,31]

$$V_{\mathrm{mix}} = S\frac{W^2}{\left(\mu_0 H-\mu_0 H_{\mathrm{res}}\right)^2+W^2}+A\frac{W\left(\mu_0 H-\mu_0 H_{\mathrm{res}}\right)}{\left(\mu_0 H-\mu_0 H_{\mathrm{res}}\right)^2+W^2}+V_{\mathrm{const}} \quad (1)$$

where S and A are the symmetric and the anti-symmetric coefficients, W is the resonance linewidth, μ_0 is the vacuum permeability, H_{res} is the resonance field, and V_{const} is an offset voltage in the measurement. The symmetric component, S, of V_{mix} is proportional to the damping-like torque generated by the spin current from the bulk VO_2 layer and the VO_2/NiFe interface, while the antisymmetric component, A, is generated by the Oersted field produced by the RF excitation current as well as the field-like torque arising from the spin current. The RF frequency dependence of H_{res} and W can be seen in Figure S2 (Supporting Information). As the sample temperature increases, the VO_2 becomes more metallic and the amount

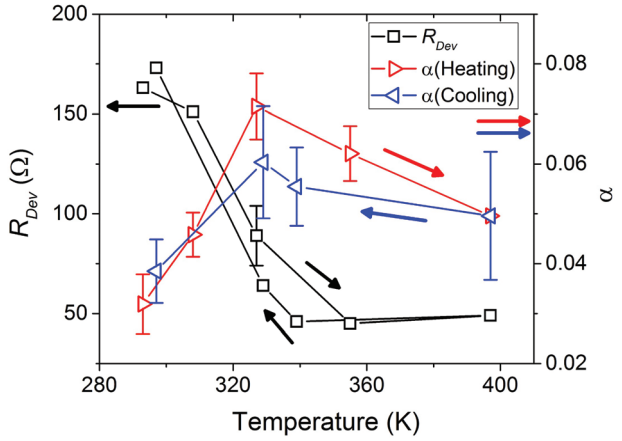

Figure 3. Temperature-depedence of device resistance and effective Gilbert damping parameter. Effective Gilbert damping parameter, α, of the VO_2/NiFe bilayer measured at different sample temperatures. To distinguish the hysteretic effects, data measured during heating (red right-tipped triangles) and cooling (blue left-tipped triangles) are indicated. The device resistance R_{Dev} (black squares) is also plotted against temperature so that the changes in α can be compared directly the insulator-metal transition of VO_2.

of the RF current through the NiFe layer that produces the V_{mix} signal decreases.

The relationship between the resonance linewidth W and the driving frequency f can be described by

$$W = W_0 + \frac{2\pi\alpha}{|\gamma|} f \tag{2}$$

where W_0 is the inhomogeneous broadening, γ is the electronic gyromagnetic ratio of NiFe (where a value of 185 GHz T^{-1} is used based on the electron Landé g-factor of 2.1[31]) and α is the effective Gilbert damping constant of the bilayer. The temperature dependence of the effective Gilbert damping parameter α, as shown in **Figure 3**, is obtained by performing the ST-FMR measurements at different temperatures. The values of α increased from (0.035 ± 0.010) at 290 K to (0.06 ± 0.01) at 355 K. The increase of α with temperature can be attributed to the combined effects of the increased magnon population in NiFe at higher temperatures and the enhanced spin current absorption[32] at the VO_2/NiFe interface as the VO_2 becomes metallic (spin pumping enhancement). The total device resistance during the same thermal cycle is also plotted in the same figure to directly compare the temperature-dependence of α and the VO_2 phase transition.

3. Temperature-Dependence of DC-Induced Spin-Orbit Torques

In this system, the next key step for functionalization is to quantify current-induced spin-orbit torques across the VO_2 phase transition. In order to examine this, we pass an additional DC current, I_{DC}, through the strip (as seen in the schematic in Figure 2b) and study how this additional stimulus affects the ST-FMR spectra, namely the linewidth W, at different temperatures. With the additional DC current, the current-induced spin-orbit torques generated in the VO_2 layer and the VO_2/NiFe interface exert damping-like torques on the precessing NiFe magnetization. Depending on the sign of the torque (which in turn depends on the directions of the current, I_{DC}, and the external magnetic field, H_{ext}), the linewidth W broadens or narrows. This can be observed in **Figure 4**a, where the application of the 1 mA (–1 mA) DC bias broadens (narrows) the linewidth W, compared to the spectrum at 0 mA. The obtained changes in the linewidth, ΔW, with our range of DC currents are a fraction of the original linewidth and comparable to the uncertainty in the linewidth estimation from the fitting according to the Equation (1). Therefore, the field sweep measurements are repeated between 20 and 50 times and the value of W are obtained by averaging. The uncertainties in W_{avg} are obtained by the statistical deviation of W, $\sigma W_{avg} = \frac{\sqrt{\Sigma_{i=1}^{N}(W_i - W_{avg})}}{N}$. The **Table 1** shows the values of W_{avg}, σW_{avg}, the number of field-sweeps and the average R^2 values for the measurements at 290 K.

The changes in the linewidth W with the added DC current are shown in Figure 4b,c at 290 K and 355 K, respectively. (The ST-FMR spectra with DC currents at different temperatures can be seen in Figure S4, Supporting Information.) The change in the linewidth is linearly proportional to the magnitude of the DC bias, indicating that the generated spin current is also linearly proportional to the applied charge current.

Remarkably, we have observed a sign change of the torques across the phase transition of VO_2, suggesting competing origins of the spin-orbit torques. Figure 4d summarizes the DC-induced linewidth changes, $\Delta W/I_{DC}$, at different temperatures, as compared to the device resistance across the phase transition. At 290 K, the VO_2 layer resistance is several orders of magnitude higher than that of the NiFe layer, and most of the applied DC current flows through the NiFe layer. The lack of the DC current flowing through the VO_2 layer eliminates the bulk spin Hall effect in the VO_2 as the main origin of the large spin-orbit torque is observed at this temperature. The effect of the self-induced torque in NiFe, as observed in Ni,[19] can explain our observed sign of the signal. Additional interfacial effects, such as inverse spin galvanic effect prominent in many Rashba-like interfaces,[15,17,33] can also additionally contribute but these effects have been reported of not having a unique sign of the generated torques. Furthermore, as the interface between the VO_2 and the NiFe is present in both the low and high temperature phases, it is not clear that strongly different inverse spin galvanic effects can be expected as a function of temperature.

As the temperature increases, VO_2 undergoes an insulator-metal transition and more current flows through the VO_2 layer (The device resistance dependence of the $\Delta W/I_{DC}$ can be found in Figure S5, Supporting Information.). Therefore, this charge current can create spin currents in the VO_2 layer by the bulk spin Hall effect, which competes with the other contributions such as the self-induced torque from NiFe or the interfacial torque. As shown in Figure 4d, the observed total spin-orbit torque decreases in magnitude with an increase in the temperature from 290 K, goes through the sign change at ≈325 K near the middle of the insulator–metal transition, then

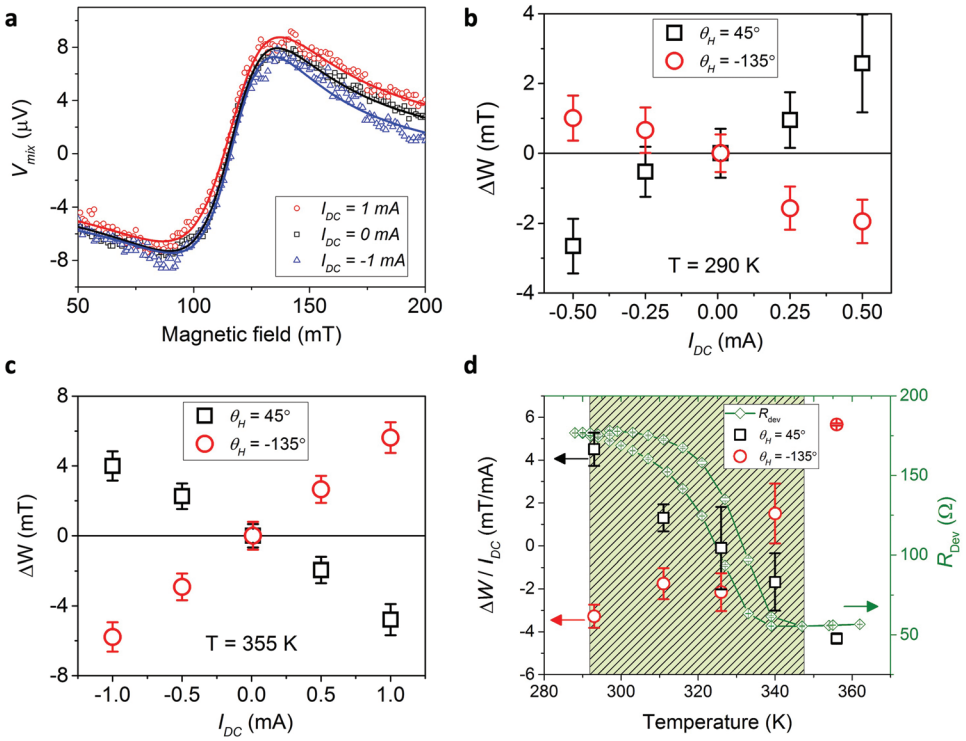

Figure 4. DC- and temperature-dependence of the linewidth modulation. a) ST-FMR field sweep data at 290 K with 8 GHz, 5dBm RF excitation at θ_H = 45° with the additional DC current, I_{DC}, of 0 mA (black), 1 mA (red) and −1 mA (blue). The solid lines are fits to the data using the Equation (1). b,c) DC-current induced linewidth change, ΔW, at 290 K (b) and 355 K (c) for θ_H = 45° (black squares) and θ_H = −135° (red circles). The lines are linear fits to the data points in each field directions. The total device resistances at 290 K and 355 K are 145 Ω and 59 Ω, respectively. d) Temperature dependence of $\Delta W/I_{DC}$ for θ_H = 45° (black square) and −135° (red circles), as compared to the device resistance (green diamonds). The light green shaded area indicates the temperature range of the insulator–metal transition.

increases again in magnitude to 355 K. The spin-orbit torque generated via the bulk spin Hall effect in the metallic VO_2 layer at 355 K is of the same sign as seen in V/CoFeB[34] and VO_2/YIG[32] (negative effective spin Hall angle).

4. First-Principles Calculation of Spin Hall Conductivity in Metallic VO_2 and Discussion

Taking into account all the above points, the large changes in the spin-orbit torque observed in our system can be interpreted by two competing mechanisms. One of the major changes brought forward by the insulator–metal transition is the electric current flowing within the VO_2 layer. In the metallic phase of the VO_2, this current in turn generates spin/orbital Hall current, which is injected into NiFe layer and thus exerts a torque. In order to estimate this effect quantitatively, we performed first-principles calculations of spin and orbital Hall conductivities of the metallic VO_2 in the rutile structure, as shown in **Figure 5**. In the figure, we show the spin Hall conductivity, σ_{SH} (blue line), and the orbital Hall conductivity, σ_{OH} (red line), as a function of the Fermi energy (E_F) with respect to the true Fermi energy (E_F^{true}), where E_F is varied assuming that the potential is fixed to the potential for E_F^{true}. The result indicates that there are two peaks for σ_{SH} near $E_F \approx E_F^{true}$. On the other hand, a peak of σ_{OH} is located at ≈ 0.3 eV above E_F^{true}. The values for the spin and orbital Hall conductivities at the true Fermi energy are σ_{SH} = −96 (ħ/e) (Ω cm)$^{-1}$ and σ_{OH} = +320 (ħ/e) (Ω cm)$^{-1}$, respectively. More details of the calculation can be found in Supporting Information Section IV. Although the orbital Hall conductivity is larger than the spin Hall conductivity, its contribution to the torque is expected to be negligible. Here, since the orbital-to-spin conversion ratio in NiFe is expected to be <10%.[20,35] We would like to point out that the sign of

Table 1. The average linewidths, errors, the number of field sweeps and the average R^2 values for the 290 K data.

DC [mA]	$W_{avg,45°}$ [mT]	$\sigma W_{avg,45°}$ [mT]	N	Average R^2	$W_{avg,-135°}$ [mT]	$\sigma W_{avg,-135°}$ [mT]	N	Average R^2
−0.5	25.2	0.4	48	0.94	27.9	0.4	49	0.96
−0.25	27.1	0.4	49	0.95	27.5	0.4	49	0.95
0.01	27.6	0.3	50	0.96	26.9	0.3	50	0.97
0.25	28.6	0.4	50	0.95	25.3	0.3	50	0.95
0.5	30.2	1.1	50	0.96	24.9	0.4	50	0.95

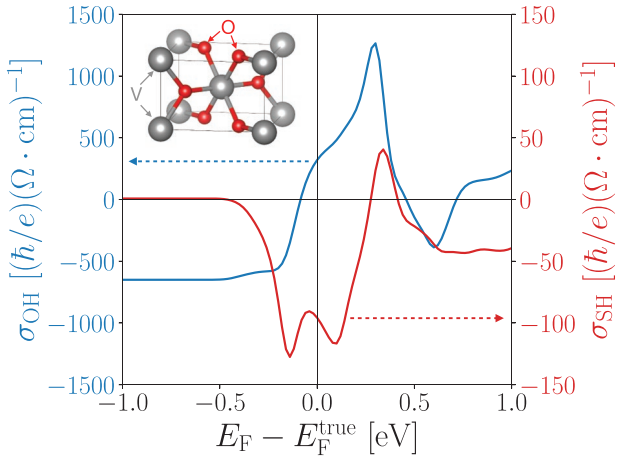

Figure 5. Spin and orbital Hall conductivity for the metallic VO_2. The crystal structure is shown in upper left, where grey and red spheres represent V and O atoms, respectively. The spin Hall conductivity (σ_{SH}) and orbital Hall conductivity (σ_{OH}) are displayed as a function of the Fermi energy (E_F) with respect to the true Fermi energy (E_F^{true}), which are indicated by solid blue and red lines, respectively. The values at E_F^{true} are $\sigma_{SH} = -96$ $(\hbar/e)$ $(\Omega\ cm)^{-1}$ and $\sigma_{OH} = +320$ $(\hbar/e)$ $(\Omega\ cm)^{-1}$, respectively.

computed spin Hall conductivity is consistent with the sign of the effective spin Hall angle measured in the experiment, which allows us to conclude that the spin Hall effect of the VO_2 is one of the main mechanisms for the torque when VO_2 is driven into the metallic phase. Meanwhile, there can be another contribution by the so-called self-induced torque/anomalous spin-orbit torque[19] in the ferromagnetic layer itself. As predicted and experimentally observed previously,[19,36] this can be interpreted as the transfer of spin angular momentum between spin-polarized charge currents and magnetization. While the spin Hall conductivity from this anomalous spin-orbit torque in NiFe itself was found to be large at ≈2300 $(\hbar/e)$ $(\Omega\ cm)^{-1}$, the value reduces to 10–100 $(\hbar/e)$ $(\Omega\ cm)^{-1}$ at an interface with a non-magnetic layer such as Cu and AlO_x, due to the additional angular momentum loss to the lattice via spin-orbit coupling. The expected magnitude and the positive sign of the spin Hall conductivity explains well the observed behavior in our NiFe/VO_2 bilayer system across the VO_2 phase transition. At the VO_2 insulating regime, the spin-orbit torque arises from the self-induced torque of the NiFe layer, while as the VO_2 becomes more metallic across the phase transition, the bulk and the negative spin Hall effect from the VO_2 dominates and reverses the spin-orbit torque direction.

Finally, there may be a contribution to the torque originating in the interfacial scattering, but we expect that the interfacial contribution does not change drastically across the insulator–metal transition since the strain induced by the structural phase transition is small (typically of ≈1%[27]).

We can now compare our results with the previous spin-pumping inverse spin Hall effect (SP-ISHE) measurements in VO_2/YIG[32]. In this system, the only source of the observed ISHE signal is the spin-to-charge conversion within the VO_2. Therefore, there is no phase-dependent reversal of the signal with temperature, but only the broadening and the reduction of the signal due to the increased interface spin-transparency at the high temperature metallic phase, which is also observed in our case as an increase in the Gilbert damping parameter α (Figure 3). In VO_2/YIG, the SP-ISHE signal is largely affected by the conductivity change of the VO_2, which is observed as a sharp decrease in the signal at high temperature. In our system, the ST-FMR signal depends on the rectified AMR effect in NiFe, whose conductivity does not change significantly across the VO_2 phase transition. This allows for the measurements of spin-orbit torques present at the VO_2/ferromagnet interface directly across the VO_2 phase transition.

As studied in depth using X-ray absorption spectroscopy,[22] the change in the VO_2 orbital occupation across the phase transition is likely to affect directly the current-induced spin-orbit torque generation mechanisms. The investigation of the orbital correlation and its effect in the spin-orbit torque at the VO_2/ferromagnet interface is reserved for a future work.

5. Conclusions

We have measured the current-induced spin-orbit torques in the VO_2/NiFe bilayer system using the spin-torque ferromagnetic resonance technique. A sign change of the damping-like spin-orbit torques with temperature is observed across the VO_2 layer phase transition. The sign change and the modulation of the observed torques with temperature suggest coexistence of various competing mechanisms, mainly the bulk spin Hall effect in metallic VO_2, corroborated by our first-principles calculation, and the self-induced torque in NiFe. While additional interfacial effects can play a role, we expect these not to change significantly across the transition, but additional measurements could be carried out to identify further possible contributions. For applications, the large (±100%) modulation, as well as the sign change of the spin-orbit torque enables full tunability of the torque to any desired value via device thermal history engineering, leading to potentially drastically different device architectures.

Supporting Information

Supporting Information is available from the Wiley Online Library or from the author.

Acknowledgements

This is a highly interactive project. The experiments were conceived jointly, and the VO_2 samples were synthesized and characterized at University of California San Diego (UCSD). The magnetic stack deposition, the ST-FMR measurements and the Hall conductivity calculations were performed at Johannes Gutenberg University Mainz (JGU Mainz) and Forschungszentrum Jülich. The manuscript was written through multiple iterations by the authors. The research at UCSD was supported by the Office of Basic Energy Science, U.S. Department of Energy, BES-DMS, and funded by the Department of Energy's Office of Basic Energy Science, DMR under grant DE FG02 87ER-45332. The work at JGU Mainz was funded by the Deutsche Forschungsgemeinshaft (DFG, German Research Foundation) – TRR 173 – 268565370 (projects A01, A11 and B02) and we acknowledge financial support from the Horizon 2020 Framework Programme of the European Commission under FET-Open grant agreement no. 863155 (s-Nebula) and ERC synergy grant agreement no. 856538 (3DMAGiC). We also gratefully acknowledge

the Jülich Supercomputing Centre and RWTH Aachen University for providing computational resources under projects jiff40 and jara0062. D.-S.H. acknowledges the support from the National Research Foundation of Korea (NRF) funded by the Ministry of Science and ICT (2020R1C1C1012664, 2019M3F3A1A02071509) and the National Research Council of Science & Technology (NST) (No. CAP-16-01-KIST). K.L. also acknowledges the support from Korea University Grant (K2111401).

Open access funding enabled and organized by Projekt DEAL.

Conflict of Interest

The authors declare no conflict of interest.

Author Contributions

M.K., I.K.S., and D.-S.H. proposed and designed the experiments. P.S., P.N.L., and N.M.V. optimized, deposited, and characterized the VO_2 samples. J.C. deposited the magnetic stack. J.K. fabricated the devices. D.-S.H., J.K., and K.L. constructed the ST-FMR measurement system. J.K. performed the ST-FMR experiments and analyzed the experimental data with help from G.J., M.K., D.G., and Y.M. performed the first-principles spin Hall conductivity calculations. J.K. wrote the manuscript through multiple iterations by all authors.

Data Availability Statement

The data that support the findings of this study are available from the corresponding author upon reasonable request.

Keywords

current-induced spin-orbit torque, insulator-metal transition, spin-torque ferromagnetic resonance, vanadium dioxide

Received: November 12, 2021
Revised: December 14, 2021
Published online: January 17, 2022

[1] G. A. Prinz, *Science* **1998**, *282*, 1660.
[2] A. Davidson,, V. P. Amin, W. S. Aljuaid, P. M. Haney, X. Fan, *Phys. Lett. A* **2020**, *384*, 126228.
[3] J. Wunderlich, B. Kaestner, J. Sinova, T. Jungwirth, *Phys. Rev. Lett.* **2005**, *94*, 047204.
[4] X. Lou, C. Adelmann, S. A. Crooker, E. S. Garlid, J. Zhang, K. S. M. Reddy, S. D. Flexner, C. J. Palmstrøm, P. A. Crowell, *Nat. Phys.* **2007**, *3*, 197.
[5] L. Liu, C.-F. Pai, Y. Li, H. W. Tseng, D. C. Ralph, R. A. Buhrman, *Science* **2012**, *336*, 555.
[6] A. Manchon, J. Železný, I. M. Miron, T. Jungwirth, J. Sinova, A. Thiaville, K. Garello, P. Gambardella, *Rev. Mod. Phys.* **2019**, *91*, 035004.
[7] I. M. Miron, K. Garello, G. Gaudin, P.-J. Zermatten, M. V. Costache, S. Auffret, S. Bandiera, B. Rodmacq, A. Schuhl, P. Gambardella, *Nature* **2011**, *476*, 189.
[8] K. Garello, C. O. Avci, I. M. Miron, M. Baumgartner, A. Ghosh, S. Auffret, O. Boulle, G. Gaudin, P. Gambardella, *Appl. Phys. Lett.* **2014**, *105*, 212402.
[9] A. Hirohata, K. Yamada, Y. Nakatani, I.-L. Prejbeanu, B. Diény, P. Pirro, B. Hillebrands, *J. Magn. Magn. Mater.* **2020**, *509*, 166711.
[10] Y. K. Kato, *Science* **2004**, *306*, 1910.
[11] J. Sinova, S. O. Valenzuela, J. Wunderlich, C. H. Back, T. Jungwirth, *Spin Hall Effects. Rev. Mod. Phys.* **2015**, *87*, 1213.
[12] J. C. R. Sánchez, L. Vila, G. Desfonds, S. Gambarelli, J. P. Attané, J. M. De Teresa, C. Magén, A. Fert, *Nat. Commun.* **2013**, *4*, 2944.
[13] S. D. Ganichev, E. L. Ivchenko, V. V. Bel'kov, S. A. Tarasenko, M. Sollinger, D. Weiss, W. Wegscheider, W. Prettl, *Nature* **2002**, *417*, 153.
[14] T. D. Skinner, K. Olejník, L. K. Cunningham, H. Kurebayashi, R. P. Campion, B. L. Gallagher, T. Jungwirth, A. J. Ferguson, *Nat. Commun.* **2015**, *6*. https://doi.org/10.1038/ncomms7730.
[15] E. Lesne, Y. Fu, S. Oyarzun, J. C. Rojas-Sánchez, D. C. Vaz, H. Naganuma, G. Sicoli, J.-P. Attané, M. Jamet, E. Jacquet, J.-M. George, A. Barthélémy, H. Jaffrès, A. Fert, M. Bibes, L. Vila, *Nat. Mater.* **2016**, *15*, 1261.
[16] A. R. Mellnik, J. S. Lee, A. Richardella, J. L. Grab, P. J. Mintun, M. H. Fischer, A. Vaezi, A. Manchon, E.-A. Kim, N. Samarth, D. C. Ralph, *Nature* **2014**, *511*, 449.
[17] M. DC, R. Grassi, J.-Y. Chen, M. Jamali, D. Reifsnyder Hickey, D. Zhang, Z. Zhao, H. Li, P. Quarterman, Y. Lv, M. Li, A. Manchon, K. A. Mkhoyan, T. Low, J.-P. Wang, *Nat. Mater.* **2018**, *17*, 800.
[18] J.-C. Rojas-Sánchez, S. Oyarzún, Y. Fu, A. Marty, C. Vergnaud, S. Gambarelli, L. Vila, M. Jamet, Y. Ohtsubo, A. Taleb-Ibrahimi, P. Le Fèvre, F. Bertran, N. Reyren, J.-M. George, A. Fert, *Phys. Rev. Lett.* **2016**, *116*, 096602.
[19] W. Wang, T. Wang, V. P. Amin, Y. Wang, A. Radhakrishnan, A. Davidson, S. R. Allen, T. J. Silva, H. Ohldag, D. Balzar, B. L. Zink, P. M. Haney, J. Q. Xiao, D. G. Cahill, V. O. Lorenz, X. Fan, *Nat. Nanotechnol.* **2019**, *14*, 819.
[20] D. Go, H.-W. Lee, *Phys. Rev. Res.* **2020**, *2*, 013177.
[21] M. Filianina, J.-P. Hanke, K. Lee, D.-S. Han, S. Jaiswal, A. Rajan, G. Jakob, Y. Mokrousov, M. Kläui, *Phys. Rev. Lett.* **2020**, *124*, 217701.
[22] N. B. Aetukuri, A. X. Gray, M. Drouard, M. Cossale, L. Gao, A. H. Reid, R. Kukreja, H. Ohldag, C. A. Jenkins, E. Arenholz, K. P. Roche, H. A. Dürr, M. G. Samant, S. S. P. Parkin, *Nat. Phys.* **2013**, *9*, 661.
[23] J. del Valle, P. Salev, F. Tesler, N. M. Vargas, Y. Kalcheim, P. Wang, J. Trastoy, M.-H. Lee, G. Kassabian, J. G. Ramírez, M. J. Rozenberg, I. K. Schuller, *Nature* **2019**, *569*, 388.
[24] H. Luo, B. Wang, E. Wang, X. Wang, Y. Sun, Q. Li, S. Fan, C. Cheng, K. Liu, *Appl. Phys. Rev.* **2019**, *6*, 041407.
[25] A. Zylbersztejn, N. F. Mott, *Phys. Rev. B* **1975**, *11*, 4383.
[26] G. Wei, X. Lin, Z. Si, N. Lei, Y. Chen, S. Eimer, W. Zhao, *Appl. Phys. Lett.* **2019**, *114*, 012407.
[27] G. Wei, X. Lin, Z. Si, D. Wang, X. Wang, X. Fan, K. Deng, K. Liu, K. Jiang, N. Lei, Y. Chen, S. Mangin, E. Fullerton, W. Zhao, *Adv. Quantum Technol.* **2020**, *3*, 1900104.
[28] X. Fan, G. Wei, X. Lin, X. Wang, Z. Si, X. Zhang, Q. Shao, S. Mangin, E. Fullerton, L. Jiang, W. Zhao, *Matter* **2020**, *2*, 1582.
[29] J. He, D. Di Sante, R. Li, X.-Q. Chen, J. M. Rondinelli, C. Franchini, *Nat. Commun.* **2018**, *9*, 492.
[30] L. Liu, T. Moriyama, D. C. Ralph, R. A. Buhrman, *Phys. Rev. Lett.* **2011**, *106*, 036601.
[31] T. Nan, S. Emori, C. T. Boone, X. Wang, T. M. Oxholm, J. G. Jones, B. M. Howe, G. J. Brown, N. X. Sun, *Phys. Rev. B* **2015**, *91*, 214416.
[32] T. S. Safi, P. Zhang, Y. Fan, Z. Guo, J. Han, E. R. Rosenberg, C. Ross, Y. Tserkovnyak, L. Liu, *Nat. Commun.* **2020**, *11*, 476.
[33] *Phys. Rev. B88*, 214417.
[34] T. Wang, W. Wang, Y. Xie, M. A. Warsi, J. Wu, Y. Chen, V. O. Lorenz, X. Fan, J. Q. Xiao, *Sci. Rep.* **2017**, *7*, 1306.
[35] D. Go, F. Freimuth, J.-P. Hanke, F. Xue, O. Gomonay, K.-J. Lee, S. Blügel, P. M. Haney, H.-W. Lee, Y. Mokrousov, *Phys. Rev. Res.* **2020**, *2*, 033401.
[36] V. P. Amin, J. Li, M. D. Stiles, P. M. Haney, *Phys. Rev. B* **2019**, *99*, 220405.